1 # The interdependence of structural and electrical properties in
2 # TiO_2/TiO/Ti periodic multilayers

3

4 Arnaud CACUCCI [(a)], Ioannis TSIAOUSSIS [(a)], Valérie POTIN [(a)], Luc IMHOFF [(a)],

5 Nicolas MARTIN [(b, c)]*, Tomas NYBERG [(c)]

6

7 [(a)] ICB - Laboratoire Interdisciplinaire Carnot de Bourgogne, UMR 6303 CNRS - Université de Bourgogne

8 9, Avenue Alain Savary, BP47870, 21078 DIJON Cedex, France

9

10 [(b)] Institut FEMTO-ST, UMR 6174, Université de Franche-Comté, CNRS, ENSMM, UTBM

11 32, Avenue de l'observatoire, 25044 BESANCON Cedex, France

12

13 [(c)] Solid State Electronics, The Ångström Laboratory, Uppsala University

14 Box 534, 75121 UPPSALA, Sweden

15

16 **Abstract**

17 Multilayered structures with 14 to 50 nm periods composed of titanium and two different
18 titanium oxides, TiO and TiO_2, were accurately produced by DC magnetron sputtering
19 using the reactive gas pulsing process (RGPP). Structure and composition of these
20 periodic TiO_2/TiO/Ti stacks were investigated by X-ray diffraction (XRD) and
21 transmission electronic microscope (TEM) techniques. Two crystalline phases hcp-Ti
22 and fcc-TiO were identified in the metallic-rich sub-layers whereas the oxygen-rich ones
23 were made of a mixture of amorphous TiO_2 and rutile phase. DC electrical resistivity ρ
24 measured for temperatures ranking from 300 to 500 K exhibited a metallic-like
25 behaviour (ρ_{473K} = 1.05×10^{-5} to 1.45×10^{-6} Ω m) with a temperature coefficient of
26 resistance (TCR) ranging from 1.20×10^{-3} K^{-1} for the highest period Λ = 50.0 nm down to

27 negative values close to -4.97×10^{-4} K^{-1} for the smallest one Λ = 14.0 nm. A relationship
28 between the dimensions of periodic layers and their collective electrical resistivity is
29 proposed where the resistivity does not solely depend on the total thickness of the film,
30 but also on the chemical composition and thickness of each sub-layer. Charge carrier
31 mobility and concentration measured by Hall effect were both influenced by the
32 dimension of TiO_2/TiO/Ti periods and the density of ionized scattering centres
33 connected to the titanium concentration in the metallic sub-layers.
34

35 **Keywords**

36 Multilayers, titanium oxides, HRTEM, periodic structure, electrical properties

37 * Corresponding author, Tel.: +33 (0)3 81 85 39 69, Fax: +33 (0)3 81 85 39 98, Email: nicolas.martin@femto-st.fr

38 **Highlights**

39 TiO_2/TiO/Ti periodic multilayers are deposited by reactive sputtering.

40 Nanometric periods from 14 to 50 nm are precisely produced by gas pulsing.

41 Hcp-Ti and fcc-TiO phases are found in the metallic sub-layers whereas amorphous and

42 rutile compounds are detected in the TiO_2 sub-layers.

43 TCR of films exhibiting metallic-like behaviour can be tuned from positive to negative.

44 Carrier mobility and concentration are connected to the density of ionized scattering

45 centres.

46 **1. Introduction**

47 For many decades, metal oxide thin films, especially titanium-based coatings, have
48 attracted much attention in various fields because of their remarkable physical, chemical
49 and biological properties. They are largely involved in a wide range of applications such
50 as antireflective coatings, gas sensors, biomedical devices, photocatalysts, etc [1-8]. In
51 addition to the intrinsic properties of titanium oxide films (metal, semiconductor,
52 insulator according to the oxygen content), some of their behaviours can also be tailored
53 playing on the nanostructure. It becomes of particular interest when the structuration is
54 performed throughout the whole thickness of the film which may be accomplished in
55 periodic metal/oxide multilayers. The resulting properties (especially the electronic
56 conductivity) can be strongly influenced by the dimensions and the quality of the
57 metal/oxide periods and interfaces. Consequently, structural and interfacial
58 characteristics have to be taken into account to understand the electronic transport
59 properties.

60 First of all, the fabrication of regular and periodic alternations appears as a relevant
61 challenge, especially with periodic multilayers involving titanium because of its strong
62 reactivity towards oxygen. Many deposition methods have been developed to prepare
63 titanium oxide films [9-15]. However, few deposition processes allow the preparation of
64 metal/oxides nanometric multilayers with abrupt and well-controlled interfaces [16-18].
65 Among these methods, the reactive sputtering may be an attractive approach to prepare
66 periodic structures at the nanometric scale. However, the reactive sputtering technique
67 normally exhibits hysteresis effects, which makes it difficult to operate the process to
68 obtain certain film compositions [19-22]. Some well-tested approaches like high
69 pumping speeds, feedback control systems or more specific devices were developed to
70 overcome the problems associated with such instabilities [23-26]. Such improvements

71 have made it possible to prepare metal oxide thin films with tuneable chemical
72 compositions.
73 In a previous work [27], the combination of DC magnetron sputtering and the reactive
74 gas pulsing process (RGPP) resulted in an accurate and reproducible structuration of
75 titanium oxide multilayers at the nanometric scale. Although these performances, the
76 idea is also to turn a sensitive material into a directly applicative and simple device for
77 gas sensors by melding electrical properties of a metal and an insulator sub-layers. Many
78 methods of gas detection can be found [28], but the simplest and the most frequently
79 used in the field of sensors is an electrical characterization by performing a resistivity
80 measurement [29]. The resistivity of a material depends among others, on the
81 temperature (this dependence is specific to the material) and is characterized by a
82 temperature coefficient of resistivity for metals. In order to obtain a temperature
83 invariant resistivity, the addition of dopant in the material is sometime required but
84 sometime leads to significant manufacture over costs. Thus, the changes of resistivity
85 could only be due to the electrical contribution of some gaseous species adsorbed at the
86 air/film interface. In TiO_2/TiO/Ti thin periodic multilayers, only the TiO_2 compound has
87 been employed as gas sensor [30]. This compound exhibits semiconducting-like
88 behaviours [31] since its resistivity exponentially decreases as a function of the
89 temperature. On the other hand, hcp-Ti and fcc-TiO are metallic phases and their
90 electrical resistivity linearly increases versus the temperature (positive temperature
91 coefficient of resistance).
92 In this article, the structural parameters of multilayered periodic TiO_2/TiO/Ti thin films
93 including the internal nanostructure evolution are investigated. These periodic stacks are
94 sputter deposited by reactive sputtering using the reactive gas pulsing process (RGPP)
95 [32]. Period of the multilayers is systematically changed from 14.0 to 50.0 nm. A study

96 of the resistivity versus temperature is performed in order to understand the relationship
97 between the electronic transport properties and the structural characteristics of the films.
98 The thickness of each sub-layer associated to the well-controlled nanometric
99 structuration produce electrical characteristics, which give rise to a metallic-like
100 behaviour with positive and negative temperature coefficients of resistance. A theoretical
101 relationship between resistivity, dimension of the TiO_2/TiO/Ti periods and chemical
102 composition is finally proposed. Charge carrier concentrations and mobilities are also
103 investigated so as to better understand their contribution in the electrical conduction
104 characteristics.
105
106 **2. Experimental details**
107 Multilayers were simultaneously deposited onto (100) Si and glass substrates by DC
108 reactive magnetron sputtering from a titanium metallic target (purity 99.6 at. % and 51
109 mm diameter) in an Ar + O_2 gas mixture. The target was sputtered with a constant
110 current density J = 100 A m^{-2}. The distance between the target and the unheated substrate
111 was fixed at 65 mm. The gas flow rates were controlled by a homemade system. All
112 depositions were carried out with an argon flow rate of 2 sccm and a constant pumping
113 speed of 13.5 L s^{-1}, which produced an argon partial pressure of 0.25 Pa. Oxygen mass
114 flow rate was periodically controlled versus time according to a rectangular signal versus
115 time by the reactive gas pulsing process, namely RGPP [32]. The pulsing period T_P of
116 the oxygen flow rate was varying from 313 to 1000 s. During each period, the flow rate
117 was periodically modulated with a t_{on} injection time which is a fraction of the total
118 period T_P. The maximum O_2 flow rate was fixed at 4 sccm during the t_{on} injection time.
119 This oxygen flow corresponds to a processing point in compound mode if the flow
120 would be kept constant. Otherwise it was completely stopped (no oxygen injection)

121 during the t_{off} time. The multilayer period thickness Λ is expected to be in-between 15 to
122 50 nm, with $\Lambda = \lambda_{met} + \lambda_{ox}$, where λ_{met} and λ_{ox} correspond to the thickness of the metal and
123 oxide sub-layers, respectively. As a result, the duty cycle α defined as the ratio t_{on}/T_P
124 takes values from 72 to 90 % in order to tune the $\lambda_{met}/\lambda_{ox}$ ratio. Moreover, the deposition
125 procedure always started with the O-rich sub-layer and finished with the Ti-rich one, the
126 total film thickness t_{tot} being close to 400 nm.
127 The crystalline structure was analyzed by X-ray diffraction (XRD) in $\theta/2\theta$ configuration
128 using a monochromatized Co Kα radiation. Scans were performed with a step of 0.02°
129 per 0.2 s and a 2θ angle ranging from 20 to 80°. Then, for all samples the local structure
130 was characterized by high resolution transmission electron microscopy (HRTEM). The
131 elemental chemical composition was determined by energy-dispersive X-ray
132 spectroscopy (EDX) with a TEM JEOL 2100 FEG operating at 200 kV (scanning probe
133 of 2 nm). The scanning technique of TEM (STEM) was used to get local and precise
134 chemical analyses at the nanometric scale, to discriminate each sub-layer, and to
135 determine their thickness. Moreover, dark field imaging was applied to provide a greater
136 contrast between the different phases.
137 DC electrical resistivity ρ of the films deposited on glass substrates was performed
138 versus temperature from 300 to 500 K with a homemade system based on the van der
139 Pauw method. In order to warrant the Ohmic behavior of the four contacts, I-V curves
140 were systematically plotted and the linear evolution was checked for all van der Pauw
141 combinations. Two cycles of measurements were carried out on each sample. The first
142 cycle started at room temperature and sample was heated up to 500 K with a ramp of 2 K
143 min^{-1} followed by a plateau for 10 min at 500 K. Afterwards, the temperature was
144 decreased with the same ramp down to 300 K and the second cycle continued with the
145 temperature profile as the first cycle. Similarly, charge carrier mobilities and

146 concentrations were obtained by Hall Effect using the same procedure as resistivity
147 measurements but applying a perpendicular magnetic field of 0.8 Tesla to the sample
148 surface.
149

150 **3. Results and discussion**

151 ***3.1 Crystallographic structure by XRD***

152 For all diffractograms (Fig. 1), two main peaks are recorded at 2θ = 33.3 and 55.5°,
153 which are attributed to the silicon (111) and (311) planes, respectively. The presence of
154 this two silicon intense peaks is due to the substrate contribution as the deposit thickness
155 is lower than 450 nm. Two other significant peaks at 2θ = 40.98 and 43.25° are also
156 detected, but they can not be related to the same crystallographic phase. For the first one,
157 an interplanar distance equal to d = 0.255 nm is obtained, which corresponds to the (100)
158 planes of the hexagonal phase of metallic titanium whereas for the second one, the
159 interplanar d-spacing is 0.241 nm. This latter is due to the (111) planes of the fcc-TiO
160 phase.
161 For the shortest period Λ = 14.0 nm, no diffracted signals are detected. The size of
162 crystalline domains is certainly lower than a couple of nanometers because the growth is
163 periodically disturbed by the pulsing introduction of the oxygen gas. The long range
164 order increases with the period thickness Λ. An increase of the peak intensity located at
165 2θ = 40.98° is clearly observed as the period Λ rises from 14.0 to 40.0 nm. It is worth
166 noticing the absence of diffracted signals corresponding to the crystalline TiO_2 phases,
167 either anatase or rutile, which are the most common phases for such kind of oxide
168 compounds. This could be explained by the weakness of the signal produced by small
169 nanocrystallites of TiO_2 (rutile or anatase phase) embedded in an amorphous TiO_2
170 matrix. In order to go further into the microstructure, TEM analyses have been carried

171 out on different locations of the mainly amorphous TiO_2 matrix and to reveal the
172 phase(s) in these nanocrystals, as it will be presented in the next paragraph.
173

174 ***3.2 Structure by TEM***

175 TEM observations on the cross-section of the different specimens show that the
176 alternation of the sub-layers is clearly visible with a regular periodic structure (Fig. 2).
177 The total thickness t_{tot} of the films is 345 and 405 nm, respectively (Fig. 2a and 2c).
178 Similarly, the total thickness t_{tot}, metallic and oxide sub-layers λ_{met} and λ_{ox}, respectively,
179 and the period Λ have been measured for all samples as reported in table 1. The sample
180 references with different periods and the Ti metal concentration are also indicated. These
181 TEM observations show that the dimension of the period stacks (two sub-layers) is
182 accurately controlled during the growth and remains constant from the substrate-film to
183 the film-air interface. TEM micrographs systematically indicate that the interface
184 between the silicon substrate and the grown multilayers is flat and regular, the thickness
185 of the native SiO_x layer being close to 3.0 nm.
186 In bright field mode (BF in figures 2a and 2c), 23 bright and dark bands alternations are
187 visible for the sample with Λ = 14.0 nm, whereas 8 bright and dark bands for the sample
188 with Λ = 50.0 nm. These bright and dark bands correspond to the oxide and metallic sub-
189 layers, respectively whereas in DF mode, it is the opposite. In dark field mode (DF), the
190 period thickness is accurately measured (± 0.1 nm) and the difference of sub-layers
191 crystallinity is evidenced (Fig. 2b and 2d). For the sample with the lowest period Λ =
192 14.0 nm, the metallic sub-layer thickness (λ_{met}) and the oxide one (λ_{ox}) is equal to 6.0 and
193 8.0 nm, respectively. DF image from the sample with Λ = 50.0 nm observed with a low
194 magnification (× 15 000) shows an alternation of wider dark and bright bands, with the
195 metallic sub-layer λ_{met} = 35.0 nm and the oxide one λ_{ox} = 15.0 nm. From our operating

196 conditions and assuming the deposition rates of titanium and titanium oxide, the period Λ
197 of such multilayers is expected to be in-between 15.0 to 50.0 nm, which is in good
198 agreement with the TEM measurements.
199 The crystalline quality of the sub-layers has also been studied in DF mode. The presence
200 of small bright domains in DF images indicates that the structure is partially
201 nanocrystalline (Fig. 2b) and that the Ti metallic sub-layer is better crystallized than the
202 oxide one (Fig. 2d). Moreover, a columnar structure is also pointed out in figure 2d, as
203 well as the presence of numerous defects close to the crystalline part. Consequently, the
204 crystallization is not homogeneous through the multilayered structure.
205 Combining EDX and DF experiments, it is possible to go further through the interface
206 characteristics between each sub-layer. It is pointed out that the darkest areas correspond
207 to the mostly amorphous oxide sub-layers (λ_{ox}), whereas the brightest ones correspond to
208 crystallized Ti-rich ones (λ_{met}). In each sample, every oxide sub-layer is composed of a
209 TiO_2 stoichiometric phase from the bottom to the top of the deposit. The titanium
210 concentration $C_{\lambda met}$ in the metallic sub-layers is kept constant in a given sample but
211 changes from a sample to another. Then, HRTEM observations confirmed that the
212 interfaces are distinguishable, and can be very flat in the less crystalline part of the
213 deposits.
214
215 ***3.3 HRTEM analyses***
216 HRTEM observations indicate that the metal/oxide periodic structure is very regular
217 through the whole thickness. The sub-layer thicknesses do not change during the growth
218 process in each period Λ as typically shown in the HRTEM micrograph for a period Λ =
219 50.0 nm (Fig. 3a). A magnified area (Fig. 3b) allows a more detailed viewing of the
220 column going through all the oxide and metallic sub-layers. It also confirms that the

221 growth continues in spite of the pulsing process. Moreover, if the growth of the metallic
222 sub-layer occurs on a column composed of crystallized TiO_2 phase (anatase or rutile), a
223 distortion phenomenon of the metallic sub-layer in the growth direction is observed,
224 which create defects and prevents the deposition of perfectly parallel multilayers to the
225 silicon surface. Selected area electron diffraction patterns (SAED) pointed out a
226 nanocrystalline structure and the presence of significant amounts of titanium-based
227 compounds in all specimens. SAED patterns are more sensitive than XRD measurements
228 to identify the different phases in a material at the nanometre scale. Indeed, this study
229 shows that the occurrence of nanocrystals increases with the thickness of the period Λ.
230 For each sample, only TiO_2 nanocrystals are present in the O-rich sub-layer λ_{ox}. The
231 crystallite size increases as function of the sub-layer thickness from $\lambda_{ox.}$ = 5.0 to 25.0
232 nm. The metal sub-layer (Ti-rich) is more crystallized and exhibits two different crystal
233 phases: hcp-Ti and fcc-TiO. Samples with small periods (Λ < 17.0 nm) are mainly
234 composed by fcc-TiO crystals in the metal sub-layers. For intermediate periods (17.0 <
235 Λ < 35.0 nm) as well as the largest (Λ > 35.0 nm) the hcp-Ti crystalline phase appears
236 (for λ_{met} > 7.0 nm), which prevails over the fcc-TiO one. This highlights that although
237 the crystallite size increases as a function of the Λ period, TiO_2 remains the only
238 crystalline phase in the O-rich sub-layer while the hcp-Ti phase becomes predominant
239 compared to the fcc-TiO one as the thickness of the metal sub-layer gradually increases.
240 In order to better understand the nanostructure, each phase and sub-layer are described in
241 more details in the next paragraphs according to some arbitrary outlines (Parts A to E) as
242 presented in figure 3b for a period Λ = 50 nm.
243
244 *3.3.1 Poorly crystallized domains – Parts A and B*
245 HRTEM micrographs show that the oxide sub-layers are mainly amorphous (part A). The

246 entire oxide sub-layer is made of more than 75 % of this amorphous part A. The
247 proportion depends on the thickness of the period Λ. When it increases from Λ = 14.0 to
248 45.0 nm, the amorphous part reduces from 95 down to 75 % (roughly estimated by
249 HRTEM). This reduction allows the development of a crystalline columnar structure
250 (TiO_2 grains) as described later for part C. In this pseudo-crystallization, an interplanar
251 distance d = 0.350 nm have been measured, which is close to the theoretical value d_{101} =
252 0.352 nm of the anatase phase. However, this measurement has only been performed for
253 few crystallographic planes and the poor occurrence of this phase is not representative to
254 the part A.
255 After this oxide sub-layer, the metallic one grows. The latter is mostly crystallized, but
256 two zones can be defined. The first zone contains the part B and is just over the A one. It
257 presents a lower content of crystallized grains than the parts D and E, which are in the
258 second zone of the metallic sub-layer. As previously described from EDS and TEM data,
259 the stacking is homogenous through the thickness λ_{met} of the metallic sub-layer. The
260 crystallinity only differs between the two zones. In the part B, HRTEM points out
261 crystallographic planes parallel to the interface of Si (100). Thus, these planes show a
262 preferential direction of growth. There are two interplanar distances, which appear
263 according to the growth direction. At first, an interplanar distance d = 0.240 nm is
264 measured and followed by another at d = 0.255 nm, which are close of the fcc-TiO phase
265 (d_{111} = 0.241 nm) and hexagonal titanium metal (d_{100} = 0.255 nm), respectively. Defects
266 in this sub-layer prevent from accurately locating the interface between these two
267 distances. In most of cases, the size of fcc-TiO grains exhibiting (111) orientation is 4.0
268 ± 0.5 nm, except for samples with Λ = 14.0 and 45.0 nm where the thickness of the fcc-
269 TiO grains is higher. However, samples with the metallic sub-layer thickness λ_{met} > 7.0
270 nm exhibit larger titanium grains with d_{100} = 0.255 nm (hcp-Ti phase) in the part B.

271

272 *3.3.2 Crystallized domains – Parts C, D and E*

273 These crystallized parts C, D and E are identified as crystalline columnar structure. The
274 width of these columns can reach 25 nm and be extended through the entire oxide sub-
275 layer thickness λ_{ox}. The C part faces the A part previously described (corresponding to
276 the O-rich sub-layer) whereas the D and E parts face the B one (Ti-rich one). Following
277 a column through those sub-layers helps to detail the different phases ocurring during the
278 growth from the oxide to the metallic sub-layer. In the complete crystalline part C of the
279 oxide sub-layer (Fig. 4d), [00-1] zone axes are indexed as a rutile-TiO_2 phase. The
280 interplanar distance d_{200} = 0.231 nm is very close to the theoretical value of 0.230 nm.
281 The crystallized zone of columns in oxide sub-layers is always composed of a rutile
282 phase, which grows in a preferential direction.

283 After the rutile TiO_2 phase, another crystallized zone is found by HRTEM. This zone
284 includes two parts (D and E). Taking into account the growing direction, zone axes
285 [01-1] of the fcc-TiO phase have been pointed out (part D) in figure 4c. Then, HRTEM
286 picture highlights that the hcp-Ti phase prevails (part E) and grows in the hexagonal
287 conformation with [001] zone axes (Fig. 4b). Thickness of the fcc-TiO phase is always
288 about 4 nm and the remaining thickness corresponds to the hcp-Ti one (except for
289 samples with Λ = 18.0 and 45.0 nm). Interplanar distances d_{111} and d_{100} (fcc-TiO and
290 hcp-Ti phases, respectively) also exhibit a preferential direction parallel to the substrate
291 surface. Moreover, the selected area electron diffraction pattern acquired in the columnar
292 area confirms that three families of planes grow following a parallel direction to each
293 other, but perpendicular to the growth direction. They are indexed as rutile-TiO_2-d_{200},
294 fcc-TiO-d_{111} and hcp-Ti-d_{100}, respectively (SAED in Fig. 4a). As a result, we can claim
295 that the multilayered structure is composed of a-TiO_2/rutile-TiO_2, fcc-TiO and hcp-Ti

296 periodic alternations. The formation of a TiO sub-layer between the TiO_2 and Ti can, to
297 some extent, be explained by the fact that it takes a certain time to sputter away the oxide
298 layer formed at the target surface. During this time, a TiO film will be grown.
299
300 ***3.4 Electrical behaviours***
301 For all samples, the DC electrical resistivity ρ was measured in the van der Pauw
302 configuration in the temperature range T = 300 – 500 K (Fig. 5). A linear evolution of ρ
303 versus T was systematically observed for any multilayer with resistivity changing from ρ
304 = 5.76×10^{-7} to 1.22×10^{-5} Ωm, which are typical of metallic-like materials. It is worth
305 noting that four samples with the shortest period Λ (χ' = 0.338 to 0.464 defined later
306 from equation (4)) exhibit a negative slope. In addition, resistivity is quasi constant for
307 sample with Λ = 40.5 nm (χ' = 0.523) whereas the others behave like conventional
308 metals, i.e. an increase of the resistivity as the temperature rises. Since the final
309 deposited sub-layer is titanium, an increase of the period thickness Λ leads to a lower
310 resistivity, which tends to that of pure titanium film. For metallic materials, the variation
311 of electrical resistivity ρ is commonly connected to the temperature T using:
312 $$\rho = \rho_0\left[1+\alpha_0\left(T-T_0\right)\right] \quad (1)$$
313 with ρ_0 is the resistivity measured at T_0 = 300 K and α_0 is the temperature coefficient of
314 resistance (TCR in K^{-1}) defined from the following relationship:
315 $$\alpha_0 = TCR = \frac{1}{\rho_0}\left[\frac{\partial\rho}{\partial T}\right]_{T=T_0} \quad (2)$$
316 As shown in table 1, positive TCR values are measured for periods Λ higher than 31.0
317 nm (except for Λ = 34.5 nm where TCR is negative). TCR ranges from 2.17×10^{-4} to
318 1.20×10^{-3} K^{-1} as the period changes from Λ = 31.0 to 50.0 nm. Resistivity as well as

319 TCR shift to the bulk Ti values for the thickest periods (ρ_{293K} = 3.91×10^{-7} Ωm and TCR

320 = 5.5×10^{-3} K^{-1} for bulk titanium). However, it significantly deviates from the bulk

321 properties as commonly observed for thin films. This is mainly attributed to the

322 scattering of electrons at the grain boundaries [33]. Thus, the decrease of conductivity

323 can be first related to the increasing number of grain boundaries per electron mean free

324 path. By decreasing the period thickness Λ, electron scattering is enhanced due to the

325 highest number of interfaces and grain boundaries since the crystallite size decreases

326 from XRD analyses (Fig. 1). It is worth noting that for the shortest periods (Λ < 16.5

327 nm), the films become amorphous. No crystallite size can be significantly determined

328 but the interfaces of the periodic TiO_2/TiO/Ti alternations are still distinguishable as

329 shown in Fig. 2a and 2b. Thus, one can assume that the scattering effect of electrons is

330 mainly due to interfaces. The electron mean free path (about few tens nanometers in well

331 crystallized films) reduces and is mainly limited by the thickness of the sub-layer periods

332 λ_{ox} and λ_{met} rather than the grain boundaries. In addition, because of the substantial

333 amount of oxygen in the metallic sub-layer, the defect concentration rises as well, which

334 contributes to the electron scattering and thus, to the high resistivity and low TCR

335 values. The defects can be point defects (vacancies, interstitials), grain boundary

336 discontinuities and 2D defects (dislocations, stacking faults) generated by interfaces of

337 the stacks. In our periodic TiO_2/TiO/Ti multilayers, the point defects are mainly oxygen

338 vacancies and titanium interstitials in the metallic sub-layer λ_{met}. A change of the

339 calculated TCR from -7.58×10^{-4} to -3.12×10^{-4} K^{-1} is even measured for the lowest

340 periods Λ although the electrical properties show a metallic-like resistivity. Such

341 negative TCRs correlate with the decrease of the grain size (tending and becoming

342 shorter than the electron mean free path) previously observed from XRD and HRTEM.

343 There variations of resistivity vs. period thickness Λ can not be solely explained taking

344 into account resistivity values of pure Ti and fcc TiO compounds (ρ_{300K}(Ti) = 3.9×10^{-7}

345 Ωm and ρ_{300K}(TiO) = 2.6×10^{-6} Ωm [34]). Our resistivity measurements showed that

346 ρ_{300K} changes from 1.2×10^{-5} down to 5.9×10^{-7} Ωm as the period thickness Λ rises from

347 14.0 to 54.0 nm, i.e. order of magnitude higher than fcc TiO compound for the shortest

348 period Λ. Thus, the sub-layer dimensions as well as the chemical composition have to be

349 taken into account.

350 In order to better understand the electrical properties of these multilayers as the period

351 thickness Λ changes, we first analyzed the correlation between the resistivity and the χ

352 parameter. This latter is defined as the metal (λ_{met}) to oxide (λ_{ox}) thickness ratio in a

353 period Λ from:

354 $$\chi = \frac{\lambda_{met}}{\lambda_{ox}} \quad (3)$$

355 In table 1, all parameters (especially the composition) are directly linked to the resistivity

356 and their corresponding TCR values. For most of the samples, the resistivity tends to

357 decrease as a function of the metallic sub-layer thickness λ_{met}. Assuming a simple

358 mixture rule [35], such a decrease can be assigned to the thickness of the metallic sub-

359 layer in the multilayer period Λ, i.e. to the χ parameter. However, the evolution of

360 resistivity at a given temperature (e.g. ρ_{475K} at 475 K as reported in table 1) versus χ

361 parameter does not exhibit a smooth trend. Multilayers with χ = 0.75, 0.69 and 0.89 (Λ =

362 14.0, 40.5 and 42.5 nm, respectively) strongly deviate from a hypothetic simple

363 exponential relationship between resistivity ρ_{475K} and the metal to oxide thickness ratio

364 χ. Such discrepancy can not be due to some variations of the total thickness of the film

365 t_{tot} since all samples are in-between 335 to 435 nm. Therefore, another and more

366 significant parameter than χ is required to link structure, composition and resistivity.

367 Taking into account EDX analyses samples, which deviates from the hypothetic

368 exponential relationship between ρ and χ stated before, titanium concentration $C_{\lambda met}$ in
369 the metallic sub-layer versus period Λ also exhibits a more or less randomized evolution.
370 The idea is then to combine the χ and $C_{\lambda met}$ parameters so as to get the real part of
371 titanium in the metallic sub-layer. For the oxide sub-layer, such correction is not relevant
372 since the chemical composition of this sub-layer is always very close to the TiO_2
373 compound for any oxide sub-layer thickness λ_{ox}. Then, the χ' parameter can be defined
374 as:

375 $$\chi' = \frac{C_{\lambda met} \times \lambda_{met}}{\lambda_{ox}} \quad (4)$$

376 It was calculated for all samples (Table 1). A regular and monotonous decrease of the
377 electrical resistivity ρ versus χ' parameter is then obtained. As a result, period Λ, sub-
378 layers thickness λ_{met} and λ_{ox} as well as titanium concentration $C_{\lambda met}$ in the metallic sub-
379 layer can be reliably connected to the resistivity. However, the total thickness t_{tot} of the
380 sample also plays an important role. Indeed, figure 6 shows a direct relationship, where ρ
381 is a function of χ' and t_{tot}. For a fixed temperature, resistivity can be expressed as:

382 $$\rho = \gamma \exp\left(\frac{\beta \, t_{total}}{\chi'}\right) \quad (5)$$

383 where γ and β are constants. It is worth noting that γ has the dimensions of an electrical
384 resistivity. Without any multilayer, one can assume that the χ' parameter approaches
385 infinity and the film can be considered as pure titanium. Then, the resistivity of the film
386 becomes that of the bulk titanium and it can be stated that γ represents the resistivity ρ_0
387 of pure Ti. From the results presented in figure 6, calculations lead to $\gamma = 5.44\times10^{-7}$ Ω m,
388 which is very close to the resistivity value measured at room temperature for the Ti pure
389 sample (5.80×10^{-7} Ω m). Similarly, $\beta = 2.97 \times10^{-7}$ m^{-1} has the dimensions of a reciprocal
390 length. In a manner analogous to the propagation of electromagnetic waves through

391 matter, its physical meaning can be similar to a virtual linear attenuation coefficient
392 intrinsic to the metal oxide interfaces created by the periodic stacks. We suggest that the
393 β parameter characterizes how easily the charge carriers can penetrate through the
394 interfaces of the multilayered structure.
395 Goldfarb et al. [36] correlated the rising resistivity in binary transition metal oxide with
396 the increasing oxygen concentration in the films. By increasing the oxygen content, they
397 claim that oxidation causes depletion of the metal d-band charge carriers in favour of the
398 O 2p valence and so, the carrier concentration decreases. A metal-insulator transition
399 occurs leading to a TCR sign change and an increase of resistivity. In our case, this
400 model can not be taken into account since the oxygen concentration is not the only
401 parameter which influences the electrical properties of TiO_2/TiO/Ti multilayers (Table
402 1). As a result, the resistivity decrease as a function of the χ' parameter has to be
403 discussed taking into account mobility and charge carriers concentration.
404 Hall effect measurements systematically reveal n-type charge carriers for all multilayers.
405 Hall mobility μ versus carrier concentration n is then plotted (Fig. 7). For all samples,
406 log μ decrease as a function of log n. At first, one can notice that mobility as well as
407 carrier concentration are both influenced by the χ' parameter. As χ' rises from 0.523 up
408 to 1.623, the carrier concentration changes from $n = 10^{22}$ to 6×10^{22} cm^{-3} and the Hall
409 mobility varies from $\mu = 5$ to 60 $cm^2V^{-1}s^{-1}$. This evolution agrees with the metallic-like
410 behaviour, which is promoted (resistivity tends to that of Ti bulk and positive sign of the
411 TCR) as χ' increases (Fig. 5). For bulk metals, electron mobility μ is in-between 10^2 to
412 10^3 $cm^2.V^{-1}.s^{-1}$ at 300 K and above room temperature, the temperature dependence
413 follows $\mu \propto T^{-1}$ [37]. For metallic thin films, electron mobility is lower than those
414 measured for bulks due to electron scattering at the grain boundaries [38], with a film's
415 thickness dependence, which is related to the nature of the metal. According to Khojier

416 and Savaloni [39], the mobility vs. thickness of pure titanium films exhibits a low
417 decrease from $\mu = 1.04\times10^3$ down to 1.00×10^3 $cm^2.V^{-1}.s^{-1}$ as the thickness rises from 12
418 up to 40 nm. From the same authors, the effect of the temperature has also been
419 investigated (from room temperature until 573 K). A decrease of the mobility (10 to 20%
420 of drop) has been observed with the temperature rising. As a result, period thickness and
421 temperature variations are in the same order of magnitude in our study. However, the
422 pure titanium properties can not be taken as the key parameter, which contributes to the
423 electronic transport properties, even for the thickest period $\Lambda = 50.0$ nm, because Hall
424 mobility of the periodic TiO_2/TiO/Ti multilayers is in-between 5 to 60 $cm^2.V^{-1}.s^{-1}$ (more
425 than one order of magnitude lower than pure titanium).
426 It is worth noting that the mobility is even more influenced by the χ' parameter changes
427 since Hall mobility exhibits values in-between $\mu = 5$ to 60 $cm^2V^{-1}s^{-1}$ as χ' rises from
428 0.523 up to 1.623, respectively. Considering the order of magnitude of the carrier
429 concentration and its evolution as a function of the carrier mobility, the electrical
430 properties are mainly related to ionized impurity scattering [40]. The theoretical
431 relationship suggested by Seto [41] for mobility dominated by grain boundary scattering
432 is negligible. The observed trend can be rather understood by the Brooks-Herring (BH)
433 theory [42]. In our study, the deposition of TiO_2/TiO/Ti periodic alternations generates
434 several types of defects, which can be point defects, grain boundary discontinuities,
435 interfacial defects (dislocations, stacking faults) and interfaces due to the multilayered
436 structure. The point defects are mainly oxygen vacancies and titanium interstitials (self-
437 interstitial atoms). As a simplifying assumption, it can be firstly assumed that such point
438 defects act as impurities in the scattering phenomena of the charge carriers. Taking into
439 account the screening of the ionized impurities, the BH theoretical relationship links
440 carrier mobility μ_{BH} ($cm^2V^{-1}s^{-1}$) and carrier concentration n (cm^{-3}) according to the

441 following equation:

442 $$\mu_{BH} = \frac{C_1}{N_{II}} T^{3/2} \left[\ln\left(C_2 \frac{T^2}{n} \right) \right]^{-1} \quad (6)$$

443 with C_1 and C_2 are constants given by:

444 $$C_1 = \frac{128\sqrt{2\pi}\,\varepsilon^2 k_B^{3/2}}{\sqrt{m_{eff}}\,Z^2 e^3} \quad (7)$$

445 and

446 $$C_2 = \frac{24\, m_{eff}\,\varepsilon\, k_B^2}{e^2 \hbar^2} \quad (8)$$

447 where T is the temperature (K), k_B the Boltzmann constant (1.38×10^{-23} JK^{-1}), Z the
448 charge of the scattering centre, ε the permittivity of the material (fixed at 6.25), m_{eff} the
449 effective mass of electron (2.28×10^{-31} kg), e the elementary charge (1.6×10^{-19} As), $\hbar$ the
450 reduced Planck's constant (1.055×10^{-34} Js) and N_{II} the ionized impurity concentration
451 (cm^{-3}). For this study, we have $C_1 = 1.0\times10^{19}$ $m^{-1}V^{-1}s^{-1}K^{-3/2}$ and $C_2 = 1.5\times10^{20}$ $m^{-3}K^{-2}$.
452 Calculations of μ_{BH} vs. n have been performed for the temperature range 300 – 500 K.
453 The carrier concentration has been incrementally increased for the studied range $n = 10^{20}$
454 - 10^{24} cm^{-3}. Increment I has been defined as a function of the carrier concentration range.
455 Hundred increments have been used for each carrier concentration decade (e.g. $I = 10^{P-2}$
456 increments with $P = 21$ for $10^{20} < n < 10^{21}$ cm^{-3}). The ionized impurity concentration N_{II}
457 was adjusted in order to fit with experimental data as shown in figure 7. It can be seen
458 that N_{II} increases from $7.30\times10^{-3}\times n$ to $4.35\times10^{-2}\times n$ cm^{-3} when the χ' parameter reduces
459 from 1.623 down to 0.523, respectively. Therefore, the decrease of μ versus n is assumed
460 to be due to an increase of the defects concentration, which act as dominant scattering
461 centres because of the fcc TiO phase occurrence in the metallic sub-layers [43]. This also
462 means that the TiO_2/TiO/Ti periodic multilayers are characterized (supported by

463 HRTEM observations) by a high stacking fault density in the range of 10^{20} cm^{-3}.
464 According to McLachlan [44], these stacking faults can mainly be generated by the
465 formation of titanium and oxygen vacancies since both types of defects can coexist over
466 a large chemical composition in the fcc-TiO_x phase ($0.8<x<1.3$). In addition, since
467 oxygen vacancies exhibit a charge of $Z = 2$, its scattering power is higher than that of
468 single ionized doping elements leading to a reduced mobility and an enhanced carrier
469 concentration.
470
471 **4. Conclusion**
472 TiO_2/TiO/Ti periodic multilayers were successfully prepared by DC reactive magnetron
473 sputtering. The reactive gas pulsing process was used to reach regular periodic
474 alternations with periods Λ in-between 14.0 and 50.0 nm. The oxide sub-layers are
475 composed of rutile and amorphous TiO_2 phases, whereas the metallic sub-layers are
476 formed by a mixture of hcp-titanium and fcc-TiO phases. The difference of metallic and
477 oxide sub-layers crystallinity was evidenced from TEM and HRTEM observations. It
478 was shown that the TiO_2/TiO/Ti periodic structure is partially nanocrystalline with
479 metallic sub-layers, which are better crystallized than the oxide ones. In the metallic sub-
480 layers, the thickness of the fcc-TiO phase was always 4 nm and the remaining
481 corresponded to hcp-Ti. A columnar structure was also pointed out with the occurrence
482 of numerous defects in the crystalline parts. HRTEM investigations confirmed that the
483 columnar growth is maintained in spite of the reactive gas pulses. The chemical
484 composition analyses revealed a homogenous TiO_2 stoichiometric compound in the
485 oxide sub-layers while the titanium concentration strongly varied in the metallic sub-
486 layers. The latter must to be taken into account to understand the electronic transport
487 properties. To this aim, a χ' parameter was defined from the titanium concentration in

488 the metallic sub-layer as well as the metal (λ_{met}) to oxide (λ_{ox}) thickness ratio in a single
489 period Λ. Such χ' parameter was connected to the DC electrical resistivity using an
490 exponential law. TiO_2/TiO/Ti periodic multilayers exhibited a metallic-like behaviour
491 with a TCR sign change and a decrease of resistivity versus χ'. It was mainly assigned to
492 a reduced carrier mobility and an enhanced carrier concentration produced by ionized
493 impurity scattering. The latter was especially favoured by an increase of the defects
494 concentration in the metallic sub-layers. Moreover, the resistivity measurements of these
495 TiO_2/TiO/Ti thin multilayers pointed out some tuneable electrical characteristics versus
496 temperature for an optimized χ' parameter. These results enable some attractive
497 applications of such multilayers, especially for sensors and devices, which often require
498 invariant conduction properties versus temperature.
499

500 **Acknowledgements**
501 This work was supported by the Region Bourgogne (PARI 2011): projet ONOV.

502 **References**

503 [1] Bange K, Ottermann CR, Anderson O, Jeschkowski U, Laube U, Feile R. Thin Solid Films
504 1991; 197:279.
505 [2] Watanabe T, Nakajima A, Wang R, Minabe M, Koizumi S, Fujishima A, Hashimoto K. Thin
506 Solid Films 1999;351:260.
507 [3] Mohammadi MR, Fray DJ. Acta Mater. 2007; 55(13):4455.
508 [4] Glassford KM, Chelikowsky JR. Phys. Rev. B 1992;46(3):1284.
509 [5] Radecka M, Rekas M, Czternastek H, Zakrzewska Z, Debrus S. Folia Phys. 1994;26:57.
510 [6] Alexandrov P, Koprinarova J, Todorov D. Vacuum 1996; 47(11):1333.
511 [7] Monoy A, Brevet A, Imhoff L, Domenichini B, Lesniewska B, Peterlé PM, Marco de Lucas
512 MC, Bourgeois S. Thin Solid Films 2006;515(2):687.
513 [8] Brevet A, Marco de Lucas MC, Potin V, Chassagnon R, Imhoff L, Domenichini B, Bourgeois
514 S. J. Phys. D: Appl. Phys. 2009;42:175302.
515 [9] Regragui M, Jousseaume V, Addou M, Outzourhit A, Bernede JC, El Idrissi B. Thin Solid
516 Films 2001;397:238.
517 [10] Manno D, Serra A, Di Giulio M, Micocci G, Tepore A. Thin Solid Films 1998;324:44.
518 [11] Fujii T, Sakata N, Takada J, Miura Y, Daitoh Y, Takano M. J. Mater. Res. 1994;9:1468.
519 [12] Takikawa H, Matsui T, Sakakibara T, Bendavid A, Martin PJ. Thin Solid Films 1999;
520 348:145.
521 [13] Zhang F, Liu X. Thin Solid Films 1998;326:171.
522 [14] Leinen D, Fernandez A, Espinos JP, Caballero A, Justo A, Gonzalez-Elipe AR. Thin Solid
523 Films 1994;241:175.
524 [15] Lobl P, Huppertz M, Mergel D. Thin Solid Films 1994;251:72.
525 [16] Elam JW, Sechrist ZA, George SM. Thin Solid Films 2002;414:43.
526 [17] Pucker G, Bellutti P, Spinella C, Gatterer K, Cazzanelli M, Pavesi L. J. Appl. Phys.
527 2000;88(10):6044.
528 [18] Switzer JA, Hung CJ, Huang LY, Miller FS, Zhou Y, Raub ER, Shumsky MG, Bohannan
529 EW. J. Mater. Res. 1998; 13(4):909.

530 [19] Hmiel AF. J. Vac. Sci. Technol. 1985; A3:592.

531 [20] Serikawa T, Okamoto A. Thin Solid Films 1983; 101:13.

532 [21] Berg S, Blom HO, Larsson T, Nender C. J. Vac. Sci. Technol. 1987;A5(2):202.

533 [22] Hoffman S. Thin Solid Films 1990; 191:335.

534 [23] Billard A, Frantz C. Surf. Coat. Technol. 1993; 59:41.

535 [24] Kusano E, Kinbara A, Baba S. J. Vac. Sci. Technol. 1992; A10 (4):1483.

536 [25] Berg S, Nyberg T. Thin Solid Films 2005; 476:215.

537 [26] Sproul WD, Rudnik PJ, Gogol CA, Mueller RA. Surf. Coat. Technol. 1989; 39-40:499.

538 [27] Cacucci A, Potin V, Imhoff L, Marco de Lucas MC, Martin N. Thin Solid Films

539 2012;520:4778.

540 [28] Sberveglieri G. Sens. Actuators B 1995; 23(2-3):103.

541 [29] Gagiotti G, Galdikas A, Kaciulis S, Mattogno G, Setkus A. J. Appl. Phys. 1994;76(8):4467.

542 [30] Tang H, Prasad K, Sanjinès R, Lévy F. Sens. Actuators B 1995; 26(1-3):71.

543 [31] Martin N, Besnard A, Sthal F, Vaz F, Nouveau C. Appl. Phys. Lett. 2008; 93(6):064102.

544 [32] Martin N, Lintymer J, Gavoille J, Chappé JM, Sthal F, Takadoum J, Vaz F, Rebouta L. Surf.

545 Coat. Technol. 2007; 201:7720.

546 [33] Reiss G, Vancea J, Hoffman H. Phys. Rev. Lett. 1986; 56(19):2100.

547 [34] Wijn HPJ, SpringerMaterials - The Landolt-Börnstein Database.

548 [35] Kasap S, Capper P. Handbook of Photonic Materials, Springer, New-York, Berlin, 2006:32.

549 [36] Goldfarb I, Miao F, Joshua Yang J, Yi W, Strachan JP, Zhang MX, Pickett MD, Medeiros-

550 Ribeiro G, Stanley Williams R. Appl. Phys. A 2012, 107:1.

551 [37] Bube RH, “Electrons in Solids”, Academic Press Inc., London, 1992.

552 [38] Chopra KL, Bahl SK, J. Appl. Phys. 1967; 38: 3607.

553 [39] Khojier K, Savaloni H, Vacuum 2010; 84: 770.

554 [40] Minami T. Thin Solid Films 2008; 516:5822.

555 [41] Seto JWY. J. Appl. Phys. 1975; 46:5247.

556 [42] Look DC. Electrical Characterization of GaAs Materials and Devices, Wiley, New-York,

557 USA, 1989; 77.

558 [43] Banakh O, Schmid PE, Sanjinès R, Lévy F. Surf. Coat. Technol. 2002; 151-152:273.

559 [44] McLachlan DS. Phys. Rev. B 1982; 25(4):2285.

560 **Table captions**

561 **Table 1**

562 Summary of dimensional, compositional and electrical characteristics of TiO_2/TiO/Ti

563 periodic multilayer films. Λ = period of TiO_2/TiO/Ti multilayers. t_{tot} = total thickness of

564 the film. λ_{met} = metallic sub-layer thickness. λ_{ox} = oxide sub-layer thickness. $\chi = \lambda_{met}/\lambda_{ox}$

565 as defined from equation (3). $C_{\lambda met}$ = titanium concentration in the metallic sub-layer. χ'

566 = $\chi \times C_{\lambda met}$ as defined from equation (4). TCR = temperature coefficient of resistance

567 calculated from equation (2). ρ_{473K} = DC electrical resistivity at 473 K.

568 **Table 1**
569

Λ	t_{tot}	λ_{met}	λ_{ox}	χ	$C_{\lambda met}$	χ'	TCR	ρ_{475K}
(± 0.1 nm)	(± 5 nm)	(± 0.1 nm)	(± 0.1 nm)	(a.u.)	(± 0.02)	(a.u.)	($\times 10^{-4}$ K^{-1})	($\times 10^{-6}$ Ωm)
14.0	345	6.0	8.0	0.75	0.45	0.338	-4.97	10.5
16.5	350	6.3	10.3	0.61	0.64	0.390	-4.17	7.25
34.6	405	15.3	19.3	0.79	0.51	0.404	-3.12	6.50
18.0	350	7.5	10.5	0.71	0.65	0.464	-7.58	5.10
40.5	325	16.5	24.0	0.69	0.76	0.523	2.17	3.40
45.0	355	24.0	21.0	1.14	0.55	0.629	2.85	2.75
42.5	335	20.0	22.5	0.89	0.75	0.667	4.76	2.53
31.0	410	17.0	14.0	1.21	0.75	0.911	3.42	2.17
40.0	435	22.5	17.5	1.29	0.80	1.029	4.55	2.02
47.3	375	29.5	17.8	1.66	0.70	1.163	10.3	1.55
50.0	405	35	15.0	2.33	0.70	1.633	12.0	1.45

570 **Figure captions**

571 **Figure 1**

572 XRD patterns of $TiO_2/TiO_x/Ti$ multilayered films deposited on (100) silicon wafer for various

573 Λ periodic alternations. The χ' parameter calculated from equation (4) is also indicated. ★ =

574 Si substrate; ● = fcc-TiO; □ hcp-Ti.

575

576 **Figure 2**

577 TEM cross-section observations of TiO_2/TiO/Ti multilayered films deposited on (100) silicon

578 wafer. a) Low magnification BF and b) DF images of the sample period Λ = 14.0 nm. The

579 thickness of metallic and oxide sub-layers is λ_{met} = 6.0 nm and λ_{ox} = 8.0 nm, respectively. The

580 total thickness is t_{tot} = 345 nm. c) Low magnification BF and d) DF images of the sample

581 period Λ = 50.0 nm with λ_{met} = 35.0 nm, λ_{ox} = 15.0 nm and t_{tot} = 405 nm.

582

583 **Figure 3**

584 a) BF micrograph of a multilayer with 8 periods of Λ = 50.0 nm and a total thickness t_{tot} = 405

585 nm. b) A magnified part of this multilayer where metallic and oxide sub-layer thicknesses are

586 λ_{met} = 35.0 nm and λ_{ox} = 15.0 nm, respectively. Poorly crystallized (A and B) and crystallized

587 domains (C, D and E) are shown.

588

589 **Figure 4**

590 (a) The selected area electron diffraction pattern reveals the epitaxial growth of TiO_2/TiO/Ti

591 multilayer, by indication of the three phases.

592 (b) HRTEM micrograph shows a part of the crystallized domains E of Fig. 3b, with an hcp-Ti
593 structure and a zone axis ZA = [0001] (c) HRTEM micrograph shows a crystalline area of the
594 part D in Fig.3b with an fcc-TiO structure and a zone axis [01-1].
595 (d) HRTEM micrograph shows a rutile phase structure with the d-spacing of the (110) and
596 (200) planes, zone axis ZA = [00-1]. A white arrow indicates the growth direction.
597
598 **Figure 5**
599 DC electrical resistivity ρ versus temperature T measured on TiO_2/TiO/Ti multilayers for
600 period thickness Λ ranging from 14.0 to 50.0 nm. The χ' parameter defined from equation (4)
601 is systematically indicated.
602
603 **Figure 6**
604 Linear evolution of the DC electrical resistivity ρ_{300K} at 300 K versus total thickness t_{tot}/χ'
605 parameter ratio. The ρ_{300K}-intercept gives the resistivity of bulk titanium and the slope is
606 related to the capacity of charges carrier to cross through the interfaces of the multilayered
607 structure.
608
609 **Figure 7**
610 Measured Hall mobility μ as a function of the carrier concentration n of . TiO_2/TiO/Ti
611 multilayers for various χ' parameters defined from equation (4). The solid lines represent the
612 μ versus n evolution calculated from the Brooks-Herring theory assuming that the mobility is
613 dominated by the ionized impurity scattering. The ionized impurity concentration N_{II} is
614 adjusted from the carrier concentration.

615 **Figure 1**

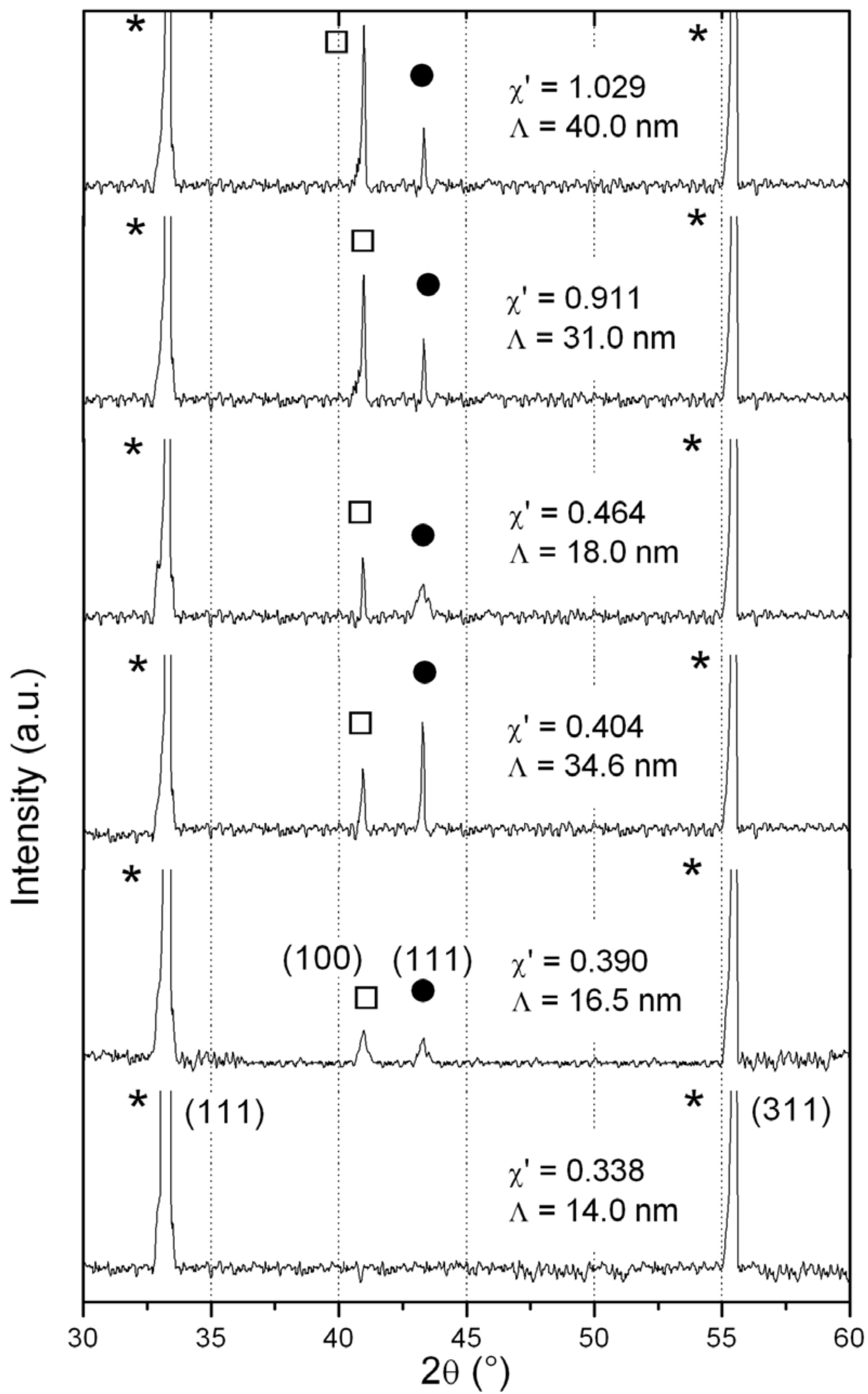

616

617 **Figure 2**

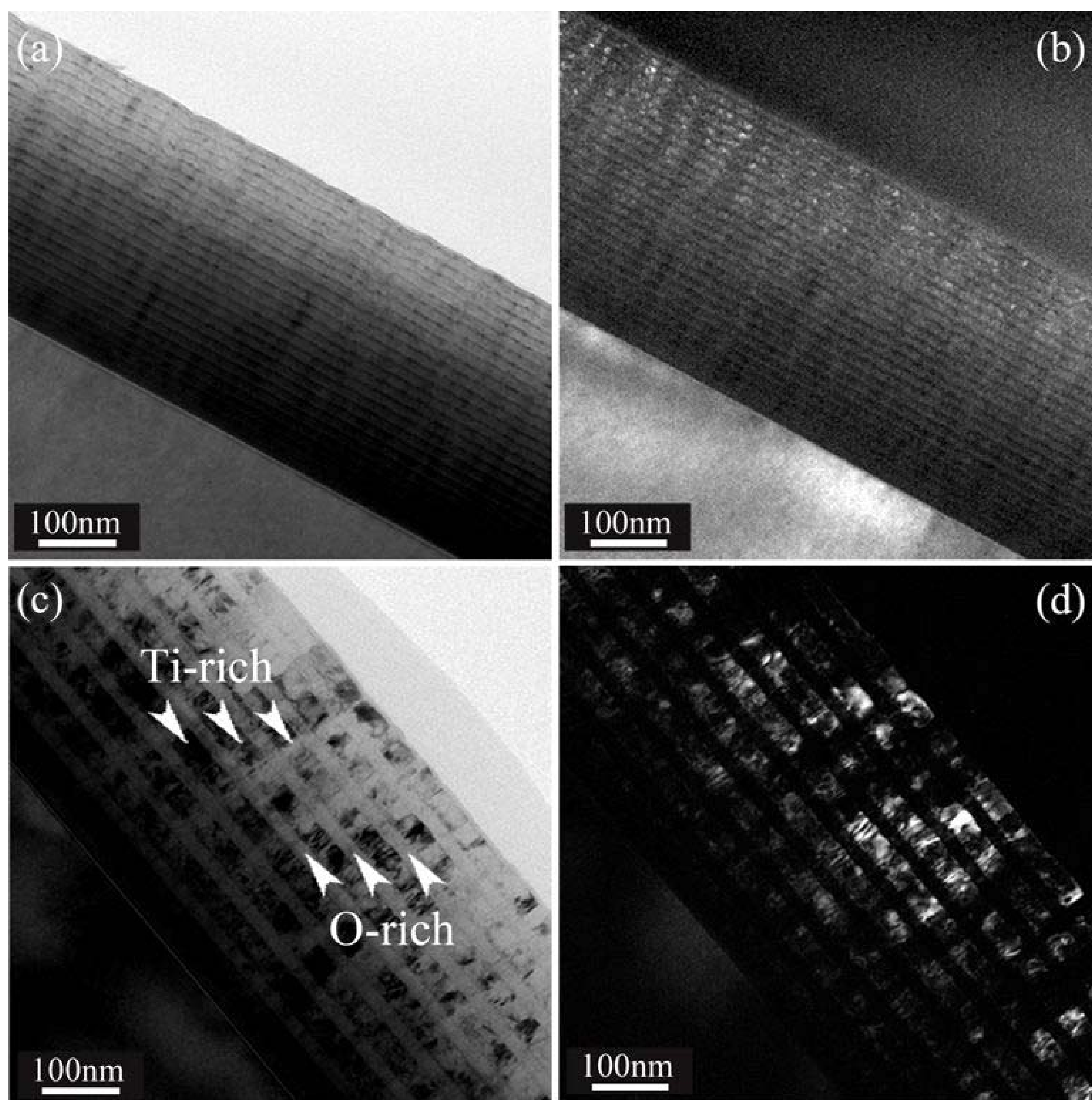

618

619 **Figure 3**

620

621 **Figure 4**

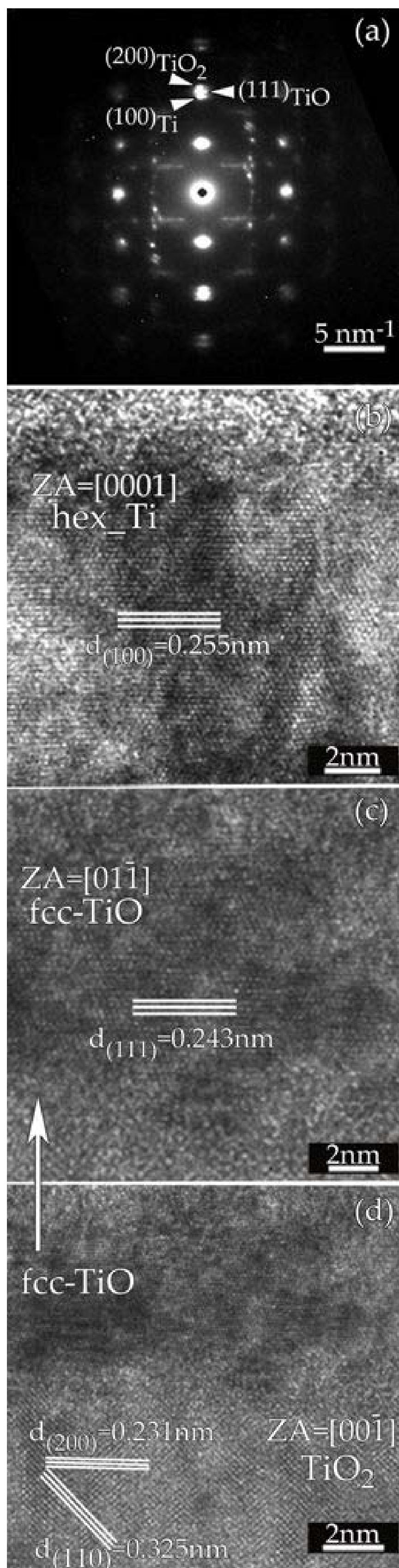

622

623 **Figure 5**

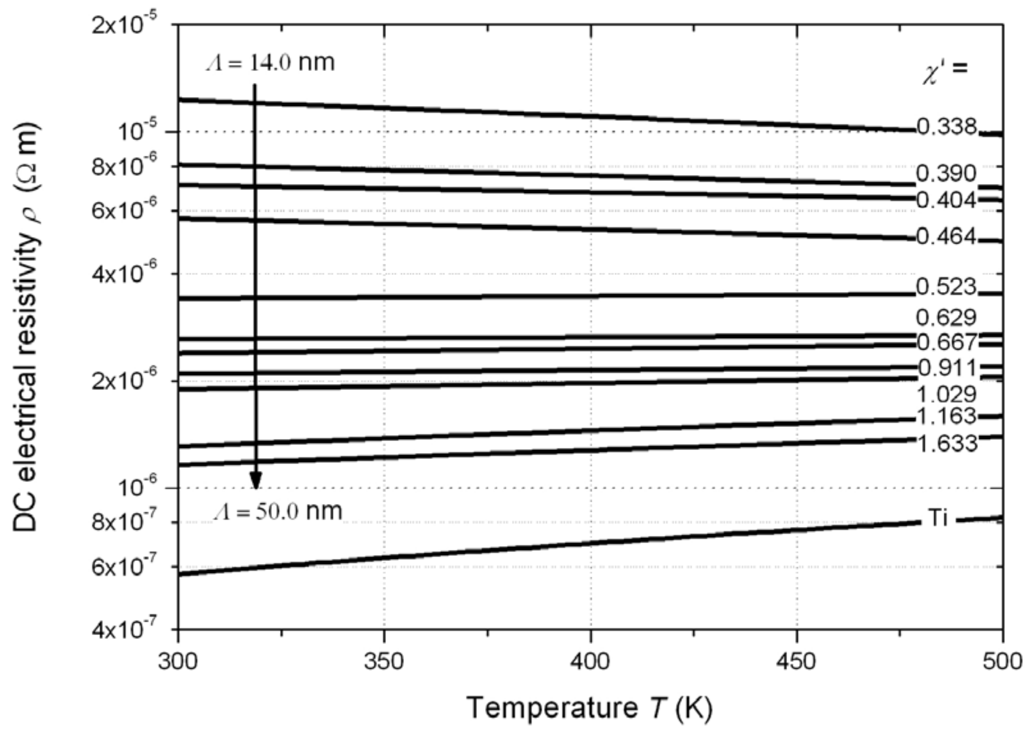

624

625 **Figure 6**

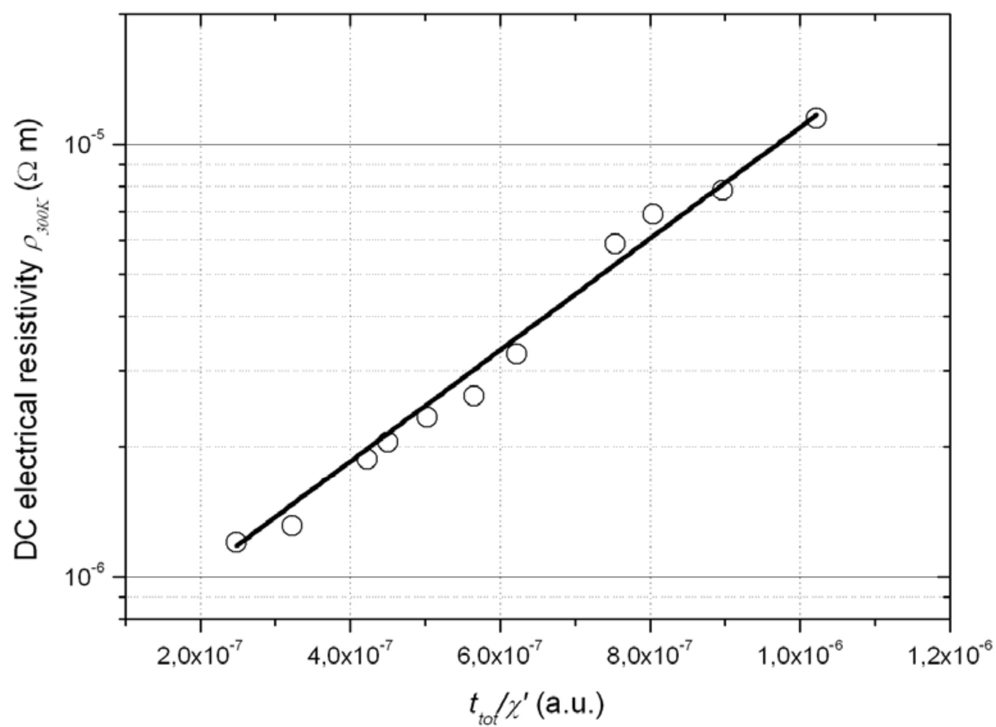

626

627 **Figure 7**

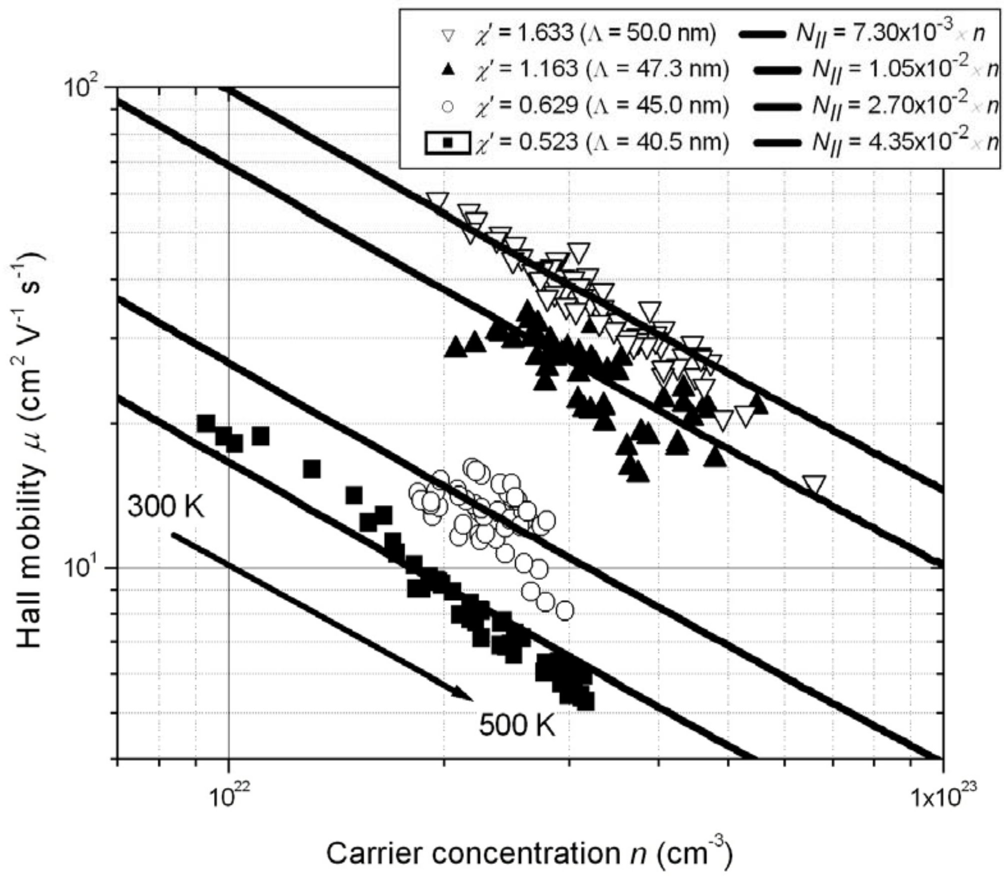

628